Cosmoglobe DR1. III. First full-sky model of polarized synchrotron emission from all *WMAP* and *Planck* LFI data

D. Watts[1]* and U. Fuskeland[1] et al.

Institute of Theoretical Astrophysics, University of Oslo, Blindern, Oslo, Norway

September 15, 2023

ABSTRACT

We present the first statistically consistent model of full-sky polarized synchrotron emission derived from the combination of all *WMAP* and *Planck* LFI frequency maps. The basis of this analysis are the end-to-end reprocessed Cosmoglobe Data Release 1 sky maps presented in a companion paper, which have significantly lower instrumental systematics than the legacy products from each experiment. We find that the resulting polarized synchrotron amplitude map has an average noise rms of $2.4\,\mu$K at 22 GHz and a smoothing scale of 2° FWHM, which is 30 % lower than the recently released BeyondPlanck model that included only LFI+*WMAP* *Ka*–*V* data, and it is 45 % lower than the raw *WMAP* *K*-band. The mean EE/BB power spectrum ratio is 0.27 ± 0.02, which agrees well with previous estimates from both *Planck* and QUIJOTE. Assuming a power law model for the synchrotron spectral energy density, we find a full-sky inverse noise-variance weighted mean of $\beta_s = -3.06 \pm 0.08$ between *WMAP* *K*-band and LFI 30 GHz, in good agreement with previous estimates. At high Galactic latitudes, however, we find $\beta_s = -3.31 \pm 0.08$, which is slightly steeper than most previous foregrounds-oriented estimates, but in good agreement with the *Planck* 2018 LFI CMB likelihood result of $\beta_s = -3.27 \pm 0.04$. For comparison, the corresponding full-sky and high-latitude estimates derived from the offical *WMAP* and LFI products are $\beta_s = -3.44 \pm 0.08$ and $\beta_s = -3.71 \pm 0.08$, respectively. These values are obviously compromised by large-scale instrumental systematics in both *WMAP* and LFI. In summary, the novel Cosmoglobe DR1 synchrotron model is both more sensitive and systematically cleaner than similar previous models, and it has a more complete error description that is defined by a set of Monte Carlo posterior samples. We believe that these products are preferable for all synchrotron-related scientific applications, including simulation, forecasting and component separation.

Key words. ISM: general – Cosmology: observations, polarization, cosmic microwave background, diffuse radiation – Galaxy: general

Contents

1. Introduction

Understanding the polarization of the cosmic microwave background (CMB) is a primary focus of observational cosmology in the coming decades. Following the success of the satellite-based COBE, *WMAP*, and *Planck* experiments, as well as sub-orbital experiments including, e.g., BICEP, ACT, SPT, Polarbear, and many others, the future LiteBIRD satellite and ground-based Simons Observatory (SO) and CMB-S4 experiments will create the most sensitive maps of the polarized sky yet, providing the most stringent constraints on primordial gravitational waves.

In the past decade, uncertainty on cosmological constraints has been limited not only by instrumental sensitivity, but by incomplete knowledge of the sky itself. These analysis difficulties have been mitigated by analyzing maps from different experiments jointly, e.g., BICEP2/Keck Array and Planck Collaborations (2015), or by designing experiments with broad frequency coverage, such as *WMAP* (Bennett et al. 2013) and *Planck* (Planck Collaboration I 2020). A major impediment to joint analyses is the difficulty of combining data with different survey strategies and incompletely characterized systematics. In order to maximize scientific throughput, one must either design an experiment that can characterize every relevant observable on its own, or jointly analyze different datasets in the same joint framework.

Worth citing Planck 2015 component separation and their inclusion of Haslam and H i data in their component separation. Additionally, DMR and WMAP data used things like DIRBE and Hα maps as foreground templates. The BeyondPlanck project achieved this joint analysis by combining external data, i.e., the Haslam 408 MHz map (Haslam et al. 1982), *WMAP* *Ka*–*V* bands, *Planck* 353 GHz in polarization, and *Planck* 857 GHz in intensity, while analyzing the *Planck* 30, 44, and 70 GHz TOD (BeyondPlanck Collaboration 2023). The *Planck* LFI ex-

* Corresponding author: D. Watts; duncanwa@astro.uio.no

periment showed that raw detector sensitivity was not enough to obtain high-fidelity sky maps; Planck Collaboration II (2020) found that the detector gain solution depended on the assumed polarization and intensity of the sky. To break this circular dependency, the BeyondPlanck framework solved for the intrinsic sky signal and instrumental parameters iteratively, providing an accurate model of the entire system with full error propagation. By leveraging external data, BeyondPlanck was able to create *Planck* LFI maps of cosmological quality, while generating a robust model of the foreground sky.

In Cosmoglobe DR1 (Watts et al. 2023a), this end-to-end framework was extended, performing a joint analysis of the same data as BeyondPlanck while adding the full *WMAP* time-ordered data. This analysis not only improved the quality of the *WMAP* maps themselves, but provided the most robust full-sky model of low frequency polarized emission available to date.

In order to make use of the synchrotron model, we require robust estimates of the spectral behavior. Fundamental behaviors, such as the spectral index as a function of frequency, spatial decorrelation, and even the functional form of the SED, are yet to be fully characterized observationally. Modern attempts have been stymied by the lack of high signal-to-noise data; de Belsunce et al. (2022), for example, find spectral indices ranging from −5 to −1, well outside of the theoretical limits of (?), given in, e.g., (?). This discrepancy is largely due to inadequate data coverage, requiring higher signal-to-noise datasets that have not yet been generated. Therefore, any conclusions about the distribution of the polarized synchrotron spectral index must be verified through multiple independent analysis methods and data choices.

While the combination of as many datasets as possible would help to constrain polarized synchrotron's large-scale properties, long-standing discrepancies complicates this. As shown in, e.g., Planck Collaboration X (2016) and Weiland et al. (2018), there are discrepancies in the polarization measurements of *WMAP* and *Planck*, partially due to unconverged gain solutions (Planck Collaboration II 2020) and poorly measured mapmaking modes (Bennett et al. 2013). BeyondPlanck Collaboration (2023) resolved the unconverged gain solution creating low-systematics LFI maps for the first time, while Watts et al. (2023b) demonstrated that the poorly measured modes in *WMAP* could be removed through joint processing, while identifying a similar systematic effect that could mimic the previously-reported effect. While Watts et al. (2023a) has demonstrated that the polarized maps from these two experiments are now consistent at the white noise level, the new maps must be validated first. As noted in, e.g., Weiland et al. (2022), simply using a different analysis pipelines can result in different estimations of the underlying frequency map. As such, we take care to appopriately marginalize over instrumental effects in our spectral analysis.

In this work, we will use the *WMAP* and LFI frequency maps generated in the Cosmoglobe DR1 analysis. We perform three separate analyses; a map and power spectrum-based analysis of the synchrotron amplitude, linear correlation within regions (T-T plots), and per-pixel Gibbs sampling.

For the power spectra, compare with, e.g., Figure 33 of Planck Collaboration IV (2018). We use the same bins as in Table C.1 of Planck Collaboration XI (2020)

2. Data products

In this paper, we investigate the spatial variation of the polarized synchrotron spectral index, with an emphasis on the comparison between legacy maps against the Cosmoglobe results. The data products used are the *WMAP* and *Planck* LFI maps, with most of the statistical weight coming from 23–33 GHz. These frequencies are low enough that we can treat them as synchrotron tracers and hence ignore thermal dust and CMB, but not so low as we need to take into account effects like Faraday rotation (Fuskeland et al. 2021). The legacy data products and the data products from the Cosmoglobe *WMAP* reanalysis (Watts et al. 2023a), are described in the two following sections.

2.1. *WMAP* and *Planck* legacy products

The *Wilkinson Microwave Anistropy Probe* (Bennett et al. 2013, *WMAP*) was a NASA-funded satellite mission that observed from August 2001 to August 2010, designed to characterize the microwave sky well enough to measure the primary CMB anisotropies across the full sky down to a resolution of 13′. Using a differential scanning strategy inspired by *COBE*/DMR, *WMAP* produced maps of the sky at 23 (*K*), 33 (*Ka*), 41 (*Q*), 61 (*V*), and 94 GHz (*W*) in both polarization and intensity (Bennett et al. 2013), with angular resolutions of 53′ at 23 GHz to 13′ at 94 GHz. The maps are available on the LAMBDA website.[1]

The *Planck* Low Frequency Instrument (LFI) produced 30, 44, and 70 GHz maps in both intensity and polarization, while the High Frequency Instrument (HFI) produced 100, 143, 217, 353 GHz maps in polarization and intensity, and 545 and 857 GHz maps in intensity alone. The LFI data in particular are similar to the *WMAP* data, with higher angular resolutions of 30′, 20′, and 13′ for 30, 44, and 70 GHz, and with higher sensitivity. Although the detector design was similar, LFI observed with a single horn, and observed in rings closely aligned with the ecliptic longitude. The legacy datasets, PR3 (Planck Collaboration I 2020) and PR4 (Planck Collaboration Int. LVII 2020), are both publicly available on the *Planck* Legacy Archive (PLA).[2]

2.2. Cosmoglobe *products*

The goal of Cosmoglobe is to perform joint end-to-end analyses on several data sets jointly, preferably beginning from raw time-ordered data (TOD). Doing this can help to break the degeneracies of the different data sets, and in general reduced the amplitude of systematic effects. The analysis in BeyondPlanck Collaboration (2023) and Watts et al. (2023a) was performed on raw TOD to cosmological parameters using the Bayesian Gibbs sampler, `Commander3`. The data products produced in these analysis account for the complex interactions between the instrument, the microwave sky, and its consistutent components self-consistently. The full products from this analysis and individual maps are available on the Cosmoglobe website.[3]

The analysis in this paper makes use of Cosmoglobe end products produced by the reanalysis of the *WMAP* and *Planck* LFI TODs (Watts et al. 2023a). This analysis produced improved *WMAP* and *Planck* LFI maps, which we will use in an analysis to compare to the legacy data. In particular, we are interested in exactly the same set of maps as in the previous section in order to be able to do a comparision study. The pixelization and angular scale are the same as for the legacy products ($N_{\rm side}$ = 64, 1° FWHM). The Cosmoglobe end products consists of a series

[1] https://lambda.gsfc.nasa.gov/product/wmap/dr5/m_products.html
[2] https://pla.esac.esa.int/
[3] https://www.cosmoglobe.uio.no/products/cosmoglobe-dr1.html

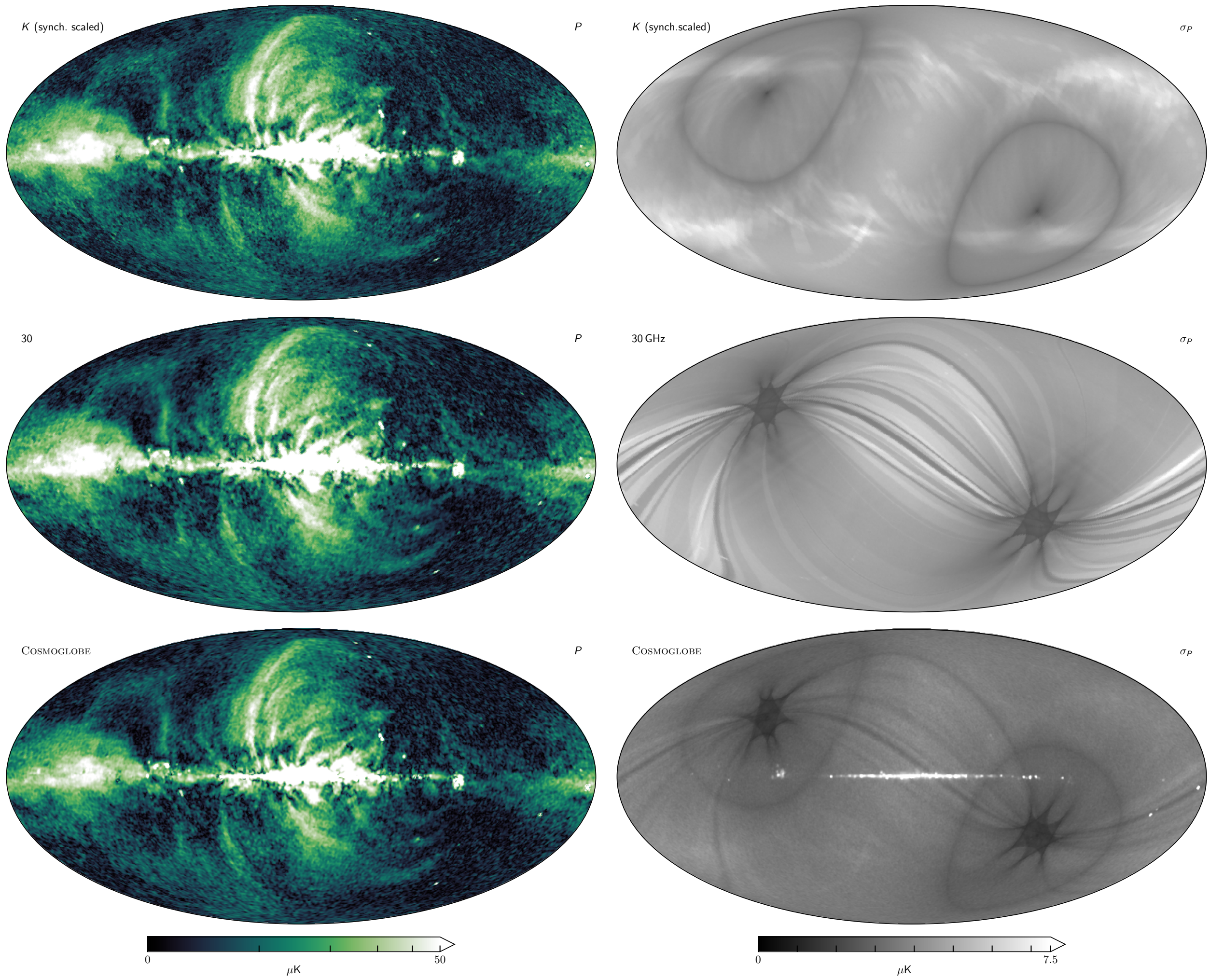

Fig. 1. Polarized intensity of *(top): WMAP K*-band, *(middle): Planck* 30 GHz, and *(bottom):* synchrotron amplitude from Cosmoglobe Gibbs chain, all evaluated at 30 GHz with a resolution of 72′. The right column shows the rms noise for the frequency maps and the posterior standard deviation of the synchrotron amplitude.

of 500 samples from the Gibbs chain, instead of just one mean sample as has been the normal case for previous data releases.

3. Polarized synchrotron amplitude

Cosmoglobe DR1 produced a sky model and instrumental parameters for each Gibbs sample, allowing for complete characterization of the dependence of low-level instrumental parameters on the sky model. The sky model includes all relevant components in *WMAP* and LFI's frequency range, specifically the CMB, synchrotron, thermal dust, free-free emission, anomalous microwave emission, and radio point sources, the first three of which are known to be polarized (radio point sources also polarized?).

When using external data for polarized foreground cleaning, the choices for high signal-to-noise full sky constraints are either *WMAP K*-band, *Planck* LFI 30 GHz, or models derived from combinations of these data, as in, e.g., Cosmoglobe. From the perspective of pure statistical uncertainty, a combination of multiple independent datasets would yield component maps that are more sensitive than each individual component. However, unmodeled systematic uncertainties in the underlying datasets, left untreated, can induce map effects that can leak into astrophysics and cosmological constraints. As shown in Watts et al. (2023a), a single sky model that all datasets are calibrated against improves the low-level instrumental processing, and allowing for degeneracies, such as poorly-measured modes in *WMAP* and differential gain uncertainty in LFI, to be broken. Within the Cosmoglobe DR1 framework, the polarization maps from *WMAP* and *Planck* LFI are consistent with each other at the 10 μK level, consistent with the instrumental white noise of the datasets.

The Cosmoglobe DR1 frequency maps are free from previously reported systematics, and are consistent between different frequencies and instruments. Therefore, a coherent model of polarized synchrotron emission can be made by combining these two different datasets. The polarized spectral amplitude determined from Cosmoglobe fully utilizes the *Planck* and *WMAP* joint reprocessed data, as shown in as shown in Fig. 1. We plot the total polarized amplitude $P = \sqrt{Q^2 + U^2}$ for ease of comparison, although it creates a visible noise bias in the low signal-to-noise regions. Much of the constraining power in the polarized synchrotron amplitude comes from (?)

While the Cosmoglobe pipeline produces samples of polarized synchrotron emission, the spatial variation of the spectral index is poorly determined within the Gibbs chain. To mitigate the poor MCMC (undefinded) convergence of the spectral indices, the Cosmoglobe DR1 sampled the spectral index from a prior distribution, $\beta_s \sim \mathcal{N}(-3.15, 0.05)$. Improvements within

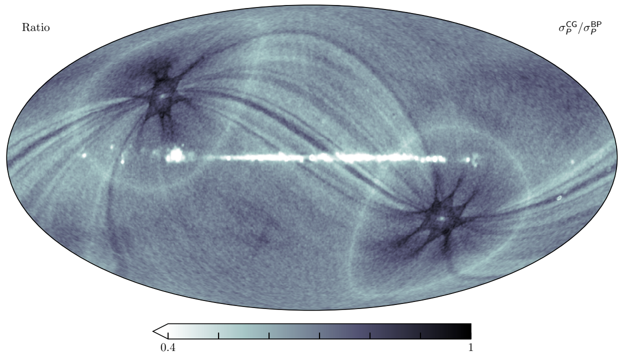

Fig. 2. Cosmoglobe posterior standard deviation divided by BeyondPlanck posterior standard deviation. The ratio is less than one for all pixels.

the `Commander3` framework will require more high signal-to-noise data and algorithmic improvements within the codebase.

The *WMAP K*-band data and LFI 30 GHz data, as the highest signal-to-noise full-sky polarized maps of Galactic synchrotron emission, are the main contributors to our knowledge of the polarized amplitude. The slightly higher angular resolution 30 GHz map has lower sensitivity than the *K*-band data, but by combining the multi-resolution maps we are able to produce a clean map of the synchrotron emission evaluated at 30 GHz with a FWHM of 1°.

The synchrotron amplitude maps from end-to-end processing, BeyondPlanck and Cosmoglobe, contain slightly different datasets, but sample the instrumental properties and sky properties jointly. Of these maps, BeyondPlanck has lower resolution and higher noise, in large part because Cosmoglobe is able to use the reprocessed *WMAP K*-band map. The Cosmoglobe synchrotron map has a mean posterior rms of 2.4 μK, a marked improvement over the BeyondPlanck map, as shown in Fig. 2. The rms map itself contains high signal-to-noise regions corresponding to the *WMAP* circles about the ecliptic poles as well as the *Planck* rings and multiple ecliptic polar crossings. The main clear astrophysical variation comes in the forms of a thin region about the Galactic plane and several low-latitude point sources. Much of the improvement can be seen more clearly when taking the ratio of the posterior rms's, as in the bottom panel of Fig. 2 (currently only one panel in Fig 2.). As expected, the regions with the lowest ratios correspond to the deep *WMAP* observations and the Galactic plane, which benefit from the high signal-to-noise of the *K*-band data. Regions with nearly identical rms include regions with the highest *Planck* depth, i.e., the ecliptic poles, and regions less deeply observed by *WMAP*, corresponding to planet crossings and artifacts from the processing mask. Notably, stripes corresponding the *Planck* scan strategy also show improvement respect to BeyondPlanck. This is due to the interaction between the sky model and LFI's instrumental parameters – with the high signal-to-noise *K*-band data, the sky model becomes more stable, and LFI's relative gain solution becomes better determined.

To quantify the noise improvement in the synchrotron maps over pure templates based on either *K*-band or 30 GHz maps, we compare the posterior standard deviation of the Cosmoglobe synchrotron map with the frequency maps' rms values. The posterior standard deviation maps are $\lesssim 1\,\mu$K for *K*-band, while temperature-to-polarization uncertainty in 30 GHz contributes at the 2 μK level (see, e.g., Watts et al. 2023a and Basyrov et al. 2023 for further details). An informative prior of $D_\ell = 200\,\mathrm{e}^{-\ell(\ell+1)\sigma^2(30')}\,\mu\mathrm{K}^2$ is applied during polarized synchrotron amplitude fitting, essentially downweighting low signal-to-noise fluctuations at angular scales $\lesssim 30'$, or $\ell \gtrsim 360$ (Svalheim et al. 2023a). Therefore, the rms noise contributions are relevant at roughly $N_{\mathrm{side}} = 128$. We additionally simulate white noise smoothed to $72'$ and scaled to 30 GHz assuming $\beta_s = -3.1$, consistent with the post-processed synchrotron map, which we display in the right column of Fig. 1.

At these resolutions, the mean rms for *K*-band and 30 GHz are 4.8 μK and 4.7 μK respectively, compared to the mean value of 3.4 μK for the Cosmoglobe DR1 synchrotron map, consistent with adding the scaled maps in quadrature. While this may seem obvious on its face, the combination of *WMAP K*-band and *Planck* 30 GHz is not straightforward due to instrumental effects that remain in the maps, notably poorly measured modes in *WMAP* (Bennett et al. 2013; Weiland et al. 2018) and gain uncertainty in *Planck* (Planck Collaboration II 2020). These effects remain in the official *WMAP9* (Bennett et al. 2013) and *Planck* PR3/PR4 (Planck Collaboration II 2020; Planck Collaboration Int. LVII 2020) maps, making combination of these datasets unsuitable for Galactic science and cosmological analyses. However, the end-to-end BeyondPlanck (BeyondPlanck Collaboration 2023) products effectively removed the gain uncertainty modes from the *Planck* LFI maps, and the Cosmoglobe DR1 results (Watts et al. 2023a) are free from the poorly measured modes. As shown in Fig. 46 of Watts et al. (2023a), the *Planck* 30 GHz and the *WMAP K*-band are consistent with each other at the 10 μK level, indicating that the maps are consistent with each other down to the white noise level.

This polarized synchrotron map, derived from consistent datasets, has a white noise level 29 % lower than both the *K*-band map and the 30 GHz map, with minimal systematic uncertainties in the posterior standard deviation. Therefore, the synchrotron map derived from the Cosmoglobe DR1 Gibbs chain should be used for the characterization and removal of polarized synchrotron emission between 23–90 GHz.

3.1. Comparison with independent datasets

As a check on the polarized synchrotron amplitude, we compare the Cosmoglobe polarized synchrotron map with the frequency maps produced in the main DR1 chain, paying special attention to maps with the highest polarized synchrotron signal-to-noise ratio, *WMAP K*- and *Ka*-band, and LFI 30 and 44 GHz. These maps should agree by virtue of being produced in the same analysis framework. We compare with the *WMAP9*, PR3, and PR4 maps. Of these, the *WMAP9* results can be considered the most independent, as the results were produced with no sky model asuptions, and were produced before the *Planck* polarized maps were publically available, thus making the analysis completely unbiased. The PR3 and PR4 maps should also be independent of the *WMAP9* results, while the PR4 results share information by virtue of the joint processing framework in which the *Planck* LFI and HFI data were produced.

Using the polarized synchrotron model generated in the main Cosmoglobe DR1 chain, we can evaluate the synchrotron emission at each frequency and compare it with the maps produced by various different processing pipelines. We evaluate the Cosmoglobe sky model using the `cosmoglobe` Python package to evaluate the sky model using the full bandpass information of each instrument.[4] Visual inspection of the data with the syn-

[4] `https://cosmoglobe.readthedocs.io/en/latest/tutorials/skymodel.html`

chrotron model subtracted and smoothed to a common 5° Gaussian beam provides a robust check on the quality of the model and the underlying data.

As shown in Watts et al. (2023a) and the first and third rows of Fig. 3, the synchrotron model matches the sky model within $5\,\mu$K across the sky, with no signature of observational artifacts in the maps. In contrast, the *WMAP*, PR3, and PR4 residuals show known observational residuals in each of the maps. In particular, the *WMAP* maps show artifacts of the poorly-measured modes due to transmission imbalance in the differential horns (Jarosik et al. 2007; Bennett et al. 2013), while the PR3 and PR4 differences mostly due to relative gain errors (Planck Collaboration II 2020; Planck Collaboration Int. LVII 2020).

The *WMAP9 K*-band residuals, and to a lesser extent the *WMAP9 Ka*-band residuals, are largely dominated by the imbalance modes, and virtually no trace of them can be found in the Cosmoglobe residuals. Most of the residuals are associated with the Galactic plane and diffuse structure uncorrelated with the *WMAP* observation strategy. The positive excess in the *Ka* Stokes Q map could be due to as yet unmitigated data processing artifacts, but we consider this unlikely, as a similar large-scale excess can also be seen in the LFI 30 and 44 GHz Stokes Q map. The LFI residuals, while much improved, still show traces residuals, especially near the Galactic center, that are somewhat correlated with the gain correction templates, but not at a level that high Galactic latitude features can be identified.

As the scale of instrumental residuals have been reduced to below the white noise level for each of the synchrotron-dominated full-sky polarization maps, we are now able to associate the residuals with potential modifications to the sky model. Specifically, the Cosmoglobe DR1 processing sampled a spatially constant β_{s} with a final mean of $\beta_{\mathrm{s}} = -3.15$. In Sec. 4, we will determine the extent to which true on-sky variation can be determined based on these maps.

3.2. Power spectra

Due to the importance of foreground removal for precise primordial gravitational wave measurement, the ratio of synchrotron B-modes to E-modes has long been studied, and has been consistently noted to be less than one (Page et al. 2007; Planck Collaboration X 2016; Planck Collaboration IV 2018). The physical mechanism for this has been discussed in the context of Galactic magnetic fields and polarized thermal dust, but similar mechanisms are likely to be in play for synchrotron polarization.

To estimate the power spectra without a noise bias, we performed a `Commander` run using half-mission splits with odd-numbered scans and even-numbered scans being analyzed in runs labeled HM1 and HM2, analogous to the *Planck* "half-mission" splits. Each of these chains were performed using the same data as in the main Cosmoglobe chain, with 200 samples each.[5] The highest quality similar half-mission splits that are publically available are from the *Planck* PR3 analysis, as discussed in Planck Collaboration IV (2018). We therefore compute power spectra from the PR3 results and compare them directly with the Cosmoglobe HM splits. We needed to run a special `Commander3` chain, splitting the TODs into half mission, with all odd-numbered scans being processed in chain "HM1", and all even-numbered scans in "HM2", and produced 200 samples each. We provide these data at `cosmoglobe.uio.no`.

We perform the power spectrum using `NaMaster` (Alonso et al. 2019) using the *Planck* 2018 common polarization mask with $f_{\mathrm{sky}} = 0.78$ and using 1° apodization. To quantify the uncertainty, we take the cross spectrum for each pair of Gibbs samples from the adjacent chain, and report the 68 % confidence intervals on this posterior. The power spectra are displayed in Fig. 4, and the standard deviation is computed using the within-bin variance of each bin, with the posterior standard deviation of the Gibbs chain added in quadrature for the Cosmoglobe spectra. Other than the very lowest and very highest multipole bins, there is good per-multipole agreement between both the PR3 and Cosmoglobe DR1 spectra.

Following Planck Collaboration IV (2018), we perform power law fits to the power spectra of the form $\mathcal{D}_{\ell}^{\mathrm{EE/BB}} = A_s^{\mathrm{EE/BB}}(\ell/80)^{\alpha}$, using multipoles $\ell \in [2, 140]$. The 68 % confidence intervals for each quantity, including the $A_s^{\mathrm{BB}}/A_s^{\mathrm{EE}}$ ratio, are reported in Table 1. The primary differences between the fits to the two datasets are $\sim 2\,\sigma$ discrepancies in the A_s^{BB} and α_s^{EE} fits, while all others are consistent within $\simeq 0.5\,\sigma$. The primary drivers of these differences are lower $\mathcal{D}_{\ell}^{\mathrm{BB}}$ and higher $\mathcal{D}_{\ell}^{\mathrm{EE}}$ in the lowest bins. These fit parameters yield a $\lesssim 2\,\sigma$ lower $A_s^{\mathrm{BB}}/A_s^{\mathrm{EE}}$ value of 0.40. While this is higher than the published value of 0.34 using the same binning and mask of Planck Collaboration IV (2018), we obtained a higher value of 0.46 using very similar processing. Despite the discrepancies between the processing in this paper and Planck Collaboration IV (2018), it is clear that the Cosmoglobe DR1 ratio is lower than that of *Planck* PR3 when processed in our framework.

Table 1. Synchrotron power spectrum estimates

	PR3	Cosmoglobe
A_s^{EE}	2.39 ± 0.07	2.35 ± 0.05
A_s^{BB}	1.09 ± 0.06	0.94 ± 0.04
$A_s^{\mathrm{BB}}/A_s^{\mathrm{EE}}$ ...	0.46 ± 0.03	0.40 ± 0.02
α_s^{EE}	-0.81 ± 0.02	-0.87 ± 0.02
α_s^{BB}	-0.80 ± 0.03	-0.81 ± 0.03

4. Polarized synchrotron spectral indices

The determination of polarized synchrotron spectral index variation across the sky has been studied in detail over the past decade using several different data combinations. Although the small-scale details vary, nearly every analysis has $\beta_{\mathrm{s}} \simeq= 2.8$ in the Galactic plane and $\beta_{\mathrm{s}} \sim -3.3$ in high Galactic latitudes (Fuskeland et al. 2014; Krachmalnicoff et al. 2018; Fuskeland et al. 2021; Weiland et al. 2022), with the exception of QUIJOTE (Rubiño-Martín et al. 2023; de la Hoz et al. 2023), who find a much flatter spectral index along the Galactic plane.

However, true spatial variations beyond the high-latitude and low-latitude regions have been difficult to determine. Both Fuskeland et al. (2014) and Weiland et al. (2022) report oscillations with Galactic longitude close to the Galactic plane, but high-latitude regions variations are more difficult to determine, and tend to depend on the specific dataset chosen and the analysis method chosen. For example, de Belsunce et al. (2022) find high-latitude spectral indices varying from −5 to −1 using 30 GHz and 70 GHz.

A fundamental challenge in spectral index estimation is due to the fact that every difference between two channels can be associated with a spectral index variation if not accounted for fully. Therefore, it is necessary to not only make sure that results are robust towards data selection, but also to ensure that differences between results are not due to instrumental effects.

[5] These products can be found at `cosmoglobe.uio.no`.

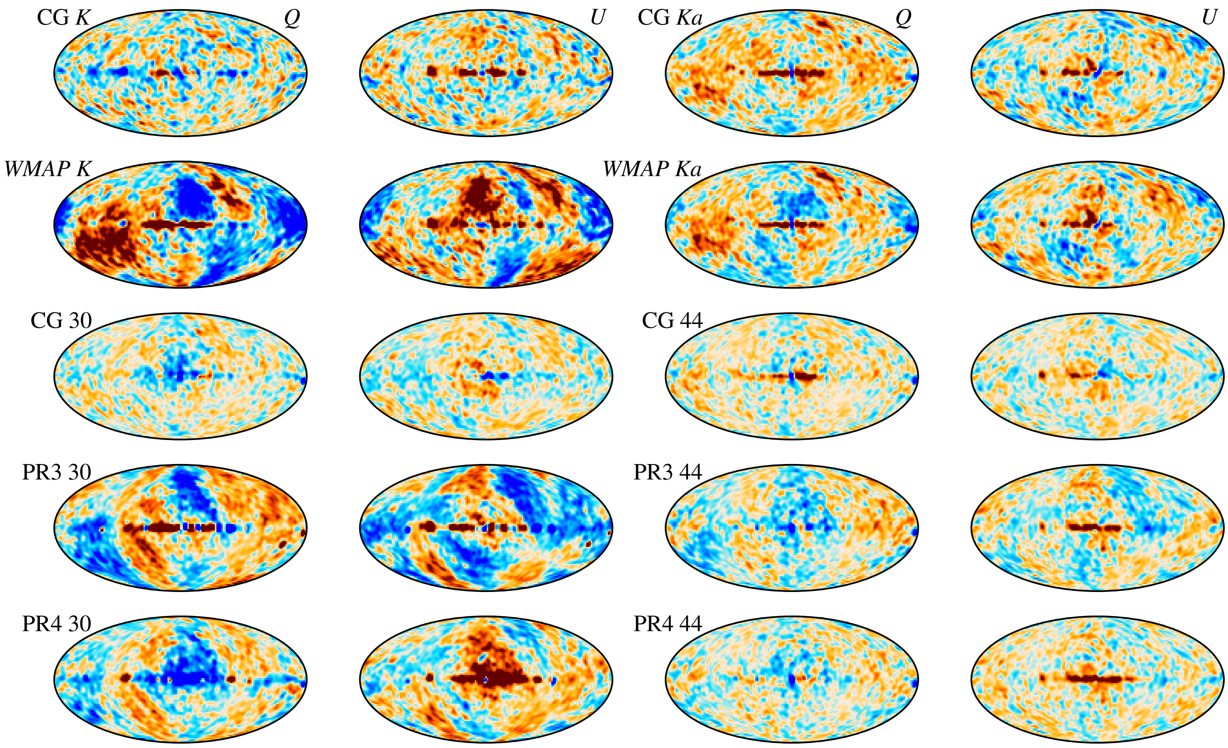

Fig. 3. Residuals with respect to the Cosmoglobe DR1 sky model evaluated at 5°, with common colorscale of ± 5 μK. Cosmoglobe maps are labeled CG, *Planck* 2018 and `NPIPE` maps are labeled PR3 and PR4, and the legacy *WMAP9* maps are labeled *WMAP*.

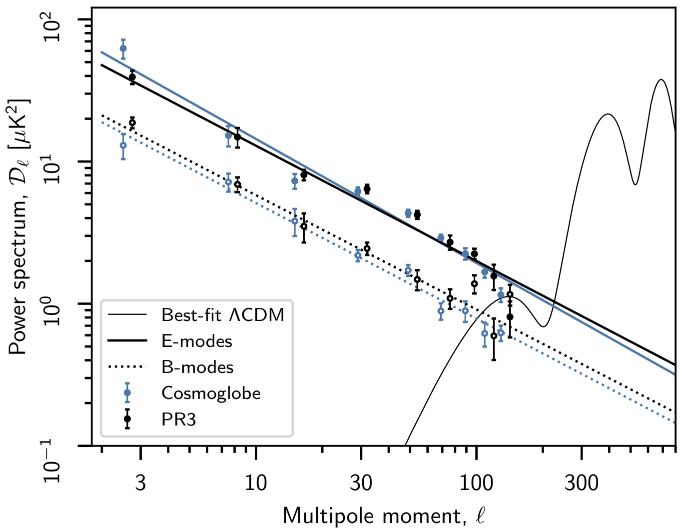

Fig. 4. Half-mission splits of synchrotron for *Planck* PR3 (black) and Cosmoglobe DR1 (black). Filled circles correspond to *E*-modes, while empty circles correspond to *B*-modes.

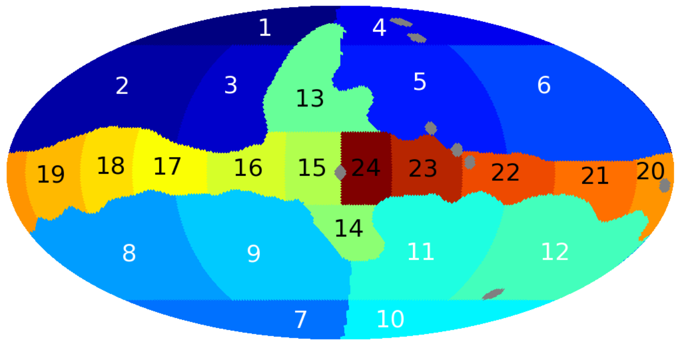

Fig. 5. The sky is split into the same 24 regions as in Fuskeland et al. (2014). The most prominent point sources are masked out and shown as the grey circular areas.

In order to test for and mitigate these effects, we perform two approaches, a T-T plot analysis in Sect. 4.1 and a Gibbs sampling analysis using `Commander1` in Sect. 4.2. Sect. 4.1 focuses on pairs of channels to better isolate potential unmodeled systematic effects, while Sect. 4.2 uses all *WMAP* and LFI channels plus *Planck* 353 GHz to maximize the joint statistical weight of all available data.

4.1. T-T plot method

As pointed out in Wehus et al. (2013), unmodeled instrumental effects, including polarization angle mismatch between detectors and elliptical beams, can induce a polarization angle-dependent spectral index that is especially prominent in point sources. These effects can often be identified by performing analysis as a function of polarization angle. As both *WMAP* and *Planck* have asymmetric beam responses, this effect has long been noticed in the data, contaminating spectral index estimates. Performing a "temperature-temperature" (T-T) analysis as a function of polarizatoin angle, as discussed in Sect. 4.1 (this section?), shows the magnitude of this effect in the Cosmoglobe, *WMAP9*, and PR4 data.

Following Fuskeland et al. (2014) and Fuskeland et al. (2021), we apply linear regression via the T-T ("temperature-

temperature") <- repetition plot method, in which spectral indices can be estimated over extended regions with approxiately constant spectral indices. In this approach, our data model for two frequencies is

$$\boldsymbol{m}_\nu = \boldsymbol{m}_{\nu_0}\left(\frac{\nu}{\nu_0}\right)^\beta + o_\nu + \boldsymbol{n}_\nu, \qquad (1)$$

where $\boldsymbol{m}_\nu$ is a spatially varying amplitude map, ν_0 is the reference frequency, β the power law between the two frequencies, o_ν the spatially constant offset per band, and $\boldsymbol{n}_\nu$ the noise. In the case of noiseleless data with no offset, the spectral index may be estimated using a simple ratio,

$$\frac{m_{\nu_1,p}}{m_{\nu_2,p}} = \left(\frac{\nu_1}{\nu_2}\right)^{\beta_{s,p}} \Rightarrow \beta_{s,p} = \frac{\ln(m_{\nu_1,p}/m_{\nu_2,p})}{\ln(\nu_1/\nu_2)}. \qquad (2)$$

The standard T-T plot method computes performs a linear regression $\boldsymbol{m}_{\nu_1} = a\boldsymbol{m}_{\nu_2} + b$, and associates β_s with $\ln a/\ln(\nu_1/\nu_2)$. More care must be taken when the noise amplitudes in both maps are comparable, so we adopt the effective variance method of Orear (1982) as implemented by Fuskeland et al. (2014).

For the T-T plot analysis, we focus exclusively on bands between 23 and 33 GHz. As in Fuskeland et al. (2014), we use the *WMAP* *K* and *Ka* band Stokes *Q* and *U* parameter maps at 23 GHz and 33 GHz. The respective effective frequencies used are 22.45 GHz and 32.64 GHz. The maps originally at a `HEALPix` pixelization of $N_{\mathrm{side}} = 512$ are downgraded to $N_{\mathrm{side}} = 64$ and smoothed to a common resolution of 1° FWHM. The *Planck* data products used are the 30 GHz Stokes *Q* and *U* maps, with an effective frequency of 28.4 GHz. also mention BeyondPlanck products, if we choose to show them. The Cosmoglobe (PR4) products are natively at $N_{\mathrm{side}} = 512$ (1024), but as for the *WMAP* products, the maps are downgraded to $N_{\mathrm{side}} = 64$ and smoothed to 1° FWHM.

The uncertainty is calculated as the minimum of the uncertainties in each rotation angle, and region. As in the Fuskeland 2021 paper, an systematic uncertainty that takes into account the variation of β over rotation angle; $[\max(\beta_\alpha) - \min(\beta_\alpha)]/2$ is added in quadrature to the statistical uncertainty. For the Cosmoglobe analyses the standard deviation of the spectral indices for all samples is also added in quadrature to represent an additional systematic uncertainty.

Much better propagation of uncertainties with a whole suite of maps.

We will also use Table 6, Figure (33) of Planck 2018 results IV Diffuse component separation

4.2. Parametric component estimation

Here we use the original `Commander1` codebase[6] to perform pixel-based component separation on maps smoothed to a common resolution of 5° and at $N_{\mathrm{side}} = 64$. For this analysis, we perform 100 pixel-based `Commander1` Gibbs samples on each of the 500 Cosmoglobe DR1 Gibbs samples. This allows us to decompose the pure statistical error assuming white noise alone for each of the 100 `Commander1` samples, while changes between each main DR1 sample show the effects of low-level instrumental processing, commonly called "systematic" uncertainty. In these analyses, we use the same polarized bands as in the main CG DR1 analysis, namely *WMAP*, *Planck* LFI, and *Planck* 353 GHz. We use a prior $\beta_\mathrm{s} \sim (-3.1, 0.1^2)$ on synchrotron, and

[6] https://github.com/Cosmoglobe/Commander1

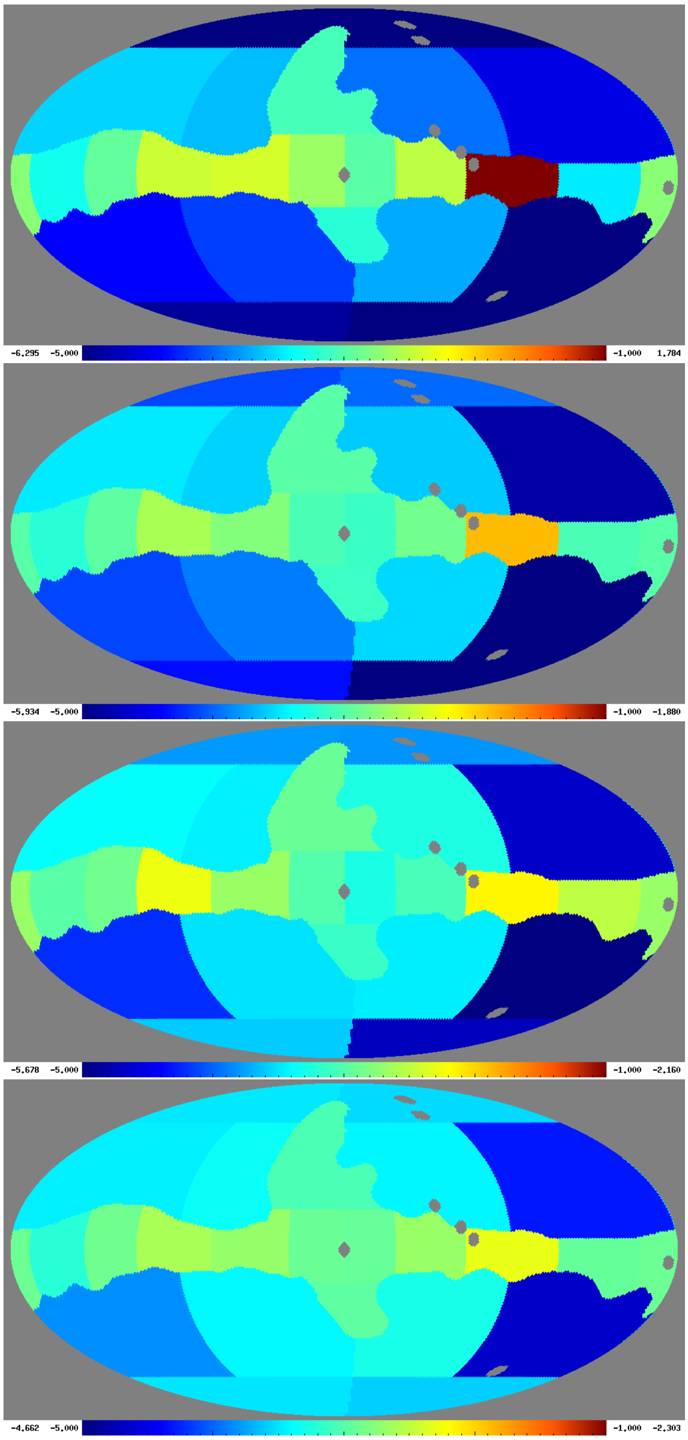

Fig. 6. The spatial variation of the synchrotron spectral index, computed using T-T plot between the (from top to bottom) *WMAP9* 23 GHz and *Planck* 2018 30 GHz, *WMAP9* 23 GHz and *Planck* DR4 30 GHz, *WMAP9* 23 GHz and BeyondPlanck 30 GHz, and Cosmoglobe 23 GHz and Cosmoglobe 30 GHz. The spectral index is inverse variance weighted over rotation angle, and in the Cosmoglobe case also samples. Fix style of maps. Also include uncertainty maps?

use a fixed dust temperature and spectral index of $T_\mathrm{d} = 21$ K and $\beta_\mathrm{d} = 1.55$ don't you use the Planck 2015 dust temperature map?).

We use the same data model as in Cosmoglobe DR1, but allow for spatially varying β_s in two different forms. First, perform a fit with β_s varying according to the pixels as in the T-T anal-

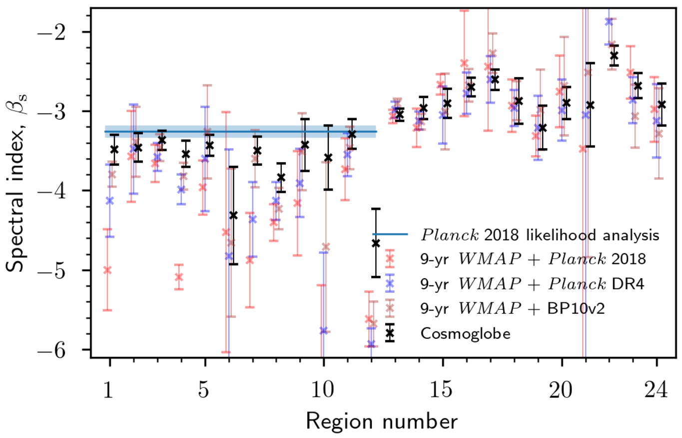

Fig. 7. The synchrotron spectral index as a function of region number, computed using T-T plot between the 9-yr *WMAP* 23 GHz and *Planck* 2018 30 GHz (red), 9-yr *WMAP* 23 GHz and *Planck* DR4 30 GHz (blue), 9-yr *WMAP* 23 GHz and BeyondPlanck 30 GHz (brown), and Cosmoglobe 23 GHz and Cosmoglobe 30 GHz (black). The spectral index is inverse variance weighted over rotation angles, and samples. The horizontal line in the high latitude regions corresponds to the estimated spectral index values from the *Planck* 2018 likelihood analysis. cite?? [Figure is a bit crowded, will discuss what to to (either remove one dataset or clean up a bit using another style (color/markers, etc).]

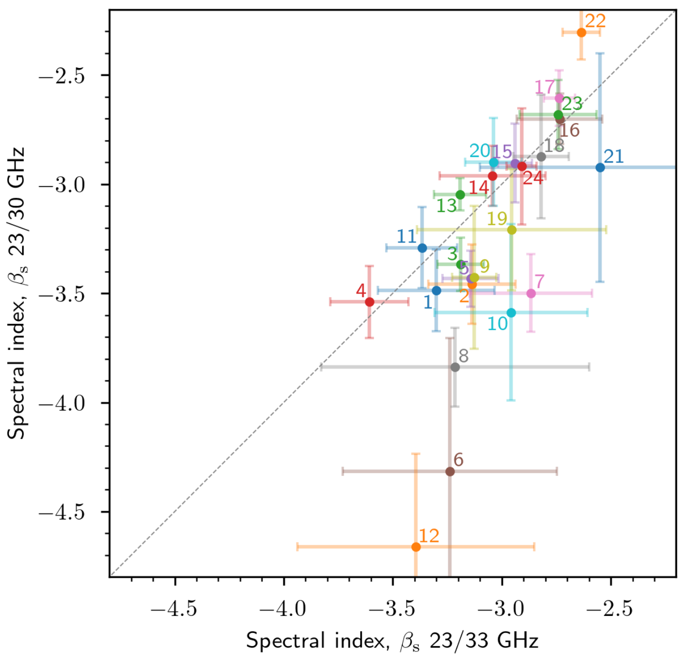

Fig. 8. The synchrotron spectral index computed using T-T plot with the Cosmoglobe 23 GHz and 30 GHz data versus Cosmoglobe 23 GHz and 33 GHz data for the 24 regions.

ysis. We find that for such large regions, there is very little effect due to the prior, and in particular find a maximum shift of 0.3 between a prior of $\mathcal{N}(-3.5, 0.1)$ and $\mathcal{N}(-2.7, 0.1)$. We add this difference in quadrature to the uncertainty due to... We also compare the reported β_s maps from QUIJOTE (de la Hoz et al. 2023) and CLASS (Eimer et al. 2023). We choose these maps because they are to this date the best publicly available available synchrotron spectral index maps available that are not affected by Faraday rotation off the Galactic plane, as in S-PASS (Krachmalnicoff et al. 2018; Fuskeland et al. 2021). The delivered β_s maps are pixelized at $N_{\rm side} = 64$ and 32, respectively, with asso-

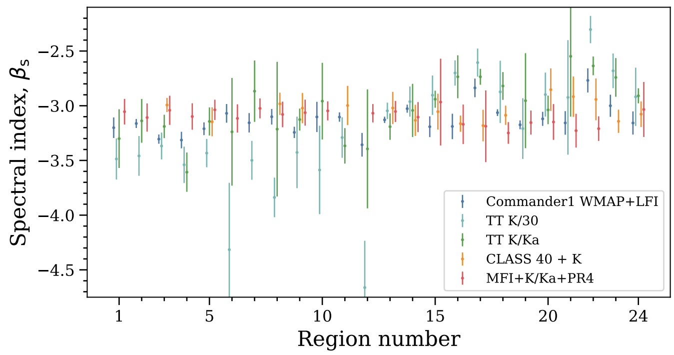

Fig. 9. Spectral index from the `Commander1`, T-T plots with *K*/*Ka* and *K*/30, the QUIJOTE estimates, and the CLASS estimates

ciated uncertainty maps taking into account the expected instrumental noise levels. We take an inverse-weighted average of the respective maps and report the weighted standard error within each region, displayed in Fig. 9.

In general, the uncertainties in the `Commander1` analysis are smaller than each of the other analyses, each for slightly different reasons. First, the T-T analyses will inherently have less constraining power than a full likelihood analysis, as this approach only uses two frequency channels via a linear regression, so the uncertainty is determined by the noise level in each frequency channel and the inherent variation within a given sky region. Beyond that, the T-T plot in this paper marginalizes over dependence on the polarization angle α, and by design accentuates systematic effects, predominantly beam ellipticity. Finally, the QUIJOTE analysis is most similar in data choice (MFI 11/13 GHz, *WMAP9 K*/*Ka*, *Planck* PR4) and methodology (`B-SeCRET`; de la Hoz et al. 2022), but still yields higher uncertainty than the `Commander1` spectral index region analysis. This is most likely due to different spatial resolution and modeling choices; the `Commander1` analysis presented here is performed at 5° resolution versus the 2° resolution per-pixel analysis in de la Hoz et al. (2023). In addition, de la Hoz et al. (2023) sampled for $\beta_{\rm d}$ and $T_{\rm d}$ with priors $\mathcal{N}(1.55, 0.1)$ and $\mathcal{N}(21, 3)$ while using a relatively wide prior on β_s of $\mathcal{N}(-3.1, 0.3)$.

At high Galactic latitudes (regions 1–12), there is good agreement between each of the treatments, and all values are consistent with a single constant value. The notable exception is the TT *K*/30 and *K*/*Ka* datapoints. As these are low signal-to-noise regions, small effects due to polarization angle rotation become even more apparent. In the North and South polar spur (regions 13 and 14) there is excellent agreement between all of the pipelines, while along the Galactic plane (regions 15–24), there are mild discrepancies between the methodologies, in particular a less distinct amount of periodic structure as a function of Galactic latitude.

To more finely probe the spatial variation of β_s, we perform a second `Commander1` analysis with identical data and model choices, except the β_s are allowed to vary with a prior of $\mathcal{N}(-3.1, 0.01)$ and spatially vary along an $N_{\rm side} = 16$ grid. We found that this was the lowest (highest resolution, lowest $N_{\rm side}$?) resolution grid in which the spectral index was not prior dominated across all high-latitude regions. In Fig. 10, we display the mean of all of the Gibbs samples, along with the standard deviation evaluated per each CG1 Gibbs sample, $\sigma_{\beta_s}^{\rm stat}$, and the standard deviation over all CG1 samples and `Commander1` samples, $\sigma_{\beta_s}^{\rm sys+stat}$. Put concretely, $\sigma_{\beta_s}^{\rm stat}$ is the standard deviation when the input maps themselves are static, and $\sigma_{\beta_s}^{sys+stat}$ includes variations in the frequency maps themselves, corresponding to underlying instrumental effects, including gain, noise characterization, and baseline estimation. The uncertainty due to white noise alone traces the high signal-to-noise regions of the polarized synchrotron, especially the prominent loops and spurs and the Fan region. At high Galactic latitudes, the standard deviation is 0.1, indicating that the posterior uncertainty is limited by the prior.

In contrast, the uncertainty across the entire Gibbs chain does not merely trace high signal-to-noise regions, and in fact there are variations that exceed the prior surrounding the Galactic center. These variations are are primarily due to gain uncertainty. It therefore makes sense that gain variations in *K*, *Ka*, and 30 GHz around the brightest region of the sky would induce a large uncertainty. Despite the relative increase in noise level when including instrumental effects, the brightest Galactic loops, the Cygnus region, and Tau A regions are well constrained by the data.

As a final quality check, we display the residuals with respect to the `Commander1` sky model in Figs. 11–12. In all bands but *K*, 30 GHz, and *Ka*, there are no visible artifacts due to instrumental uncertainty, with each map showing fluctuations consistent with the estimated white noise level calculated in the DR1 processing. In addition, many of the residuals visible in Fig. 3 have been reduced, demonstrating that polarized synchrotron spectral index variation provides meaningful improvements to the sky model fit.

The most salient remaining residuals are in *K*, 30 GHz, and *Ka*. *K*-band and 30 GHz are anticorrelated surrounding Galactic center, indicating tension between these two high signal-to-noise datasets. This could either by due to genuine mismodelling of the sky, or be due to incompletely modelled instrumental parameters. In particular, the signature is reminiscent of bandpass leakage corrections, which are shown, e.g., in Fig. 9 of Svalheim et al. (2023b).

A more persistent residual is found in the the Stokes *Q Ka*-band map. This fog has appeared in several different analyses, e.g., Fig. 4 of Svalheim et al. (2023a) and Fig. 8 of Weiland et al. (2022), but was not as clear without full removal the poorly measured modes in the final map. The lack of this feature in the corresponding Stokes *U* map suggests that the effect is not a true Galactic effect, and is in some way due to instrumental processing, or unmodeled systematics. As of writing, we have not identified any instrumental effect that, when projected on the sky, induces this excess.

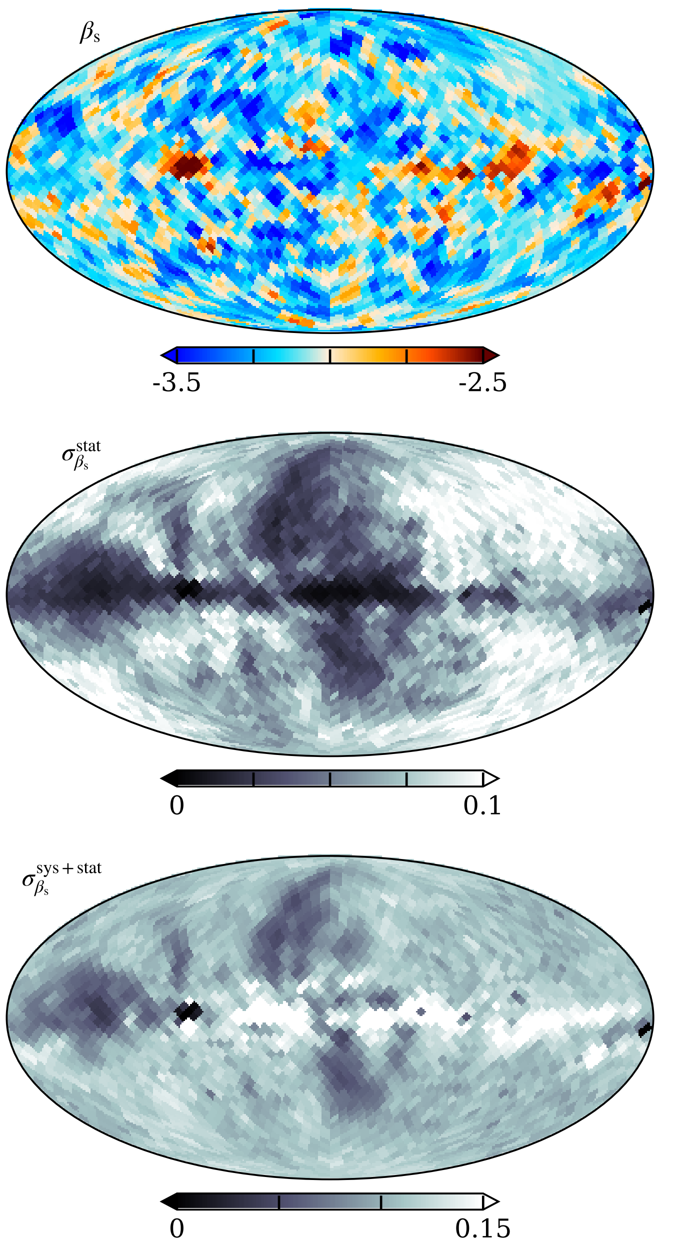

Fig. 10. `Commander1` β_s constraints. *(Top):* Mean spectral index over all samples, *(middle):* standard deviation over a single CG DR1 sample, and *(bottom):* standard deviation over all `Commander1` and CG DR1 samples. Note the different dynamic ranges in the middle and bottom figures.

5. Discussion and conclusion

References

Alonso, D., Sanchez, J., Slosar, A., & LSST Dark Energy Science Collaboration. 2019, MNRAS, 484, 4127
Basyrov, A., Suur-Uski, A.-S., Colombo, L. P. L., et al. 2023, A&A, 675, A10
Bennett, C. L., Larson, D., Weiland, J. L., et al. 2013, ApJS, 208, 20
BeyondPlanck Collaboration. 2023, A&A, 675, A1
BICEP2/Keck Array and Planck Collaborations. 2015, Phys. Rev. Lett., 114, 101301
de Belsunce, R., Gratton, S., & Efstathiou, G. 2022, MNRAS, 517, 2855
de la Hoz, E., Barreiro, R. B., Vielva, P., et al. 2023, MNRAS, 519, 3504
de la Hoz, E., Diego-Palazuelos, P., Martínez-González, E., et al. 2022, J. Cosmology Astropart. Phys., 2022, 032
Eimer, J. R., Li, Y., Brewer, M. K., et al. 2023, arXiv e-prints, arXiv:2309.00675
Fuskeland, U., Andersen, K. J., Aurlien, R., et al. 2021, A&A, 646, A69
Fuskeland, U., Wehus, I. K., Eriksen, H. K., & Næss, S. K. 2014, ApJ, 790, 104
Haslam, C. G. T., Salter, C. J., Stoffel, H., & Wilson, W. E. 1982, A&AS, 47, 1
Jarosik, N., Barnes, C., Greason, M. R., et al. 2007, ApJS, 170, 263
Krachmalnicoff, N., Carretti, E., Baccigalupi, C., et al. 2018, A&A, 618, A166
Orear, J. 1982, American Journal of Physics, 50, 912
Page, L., Hinshaw, G., Komatsu, E., et al. 2007, ApJS, 170, 335
Planck Collaboration X. 2016, A&A, 594, A10
Planck Collaboration I. 2020, A&A, 641, A1
Planck Collaboration II. 2020, A&A, 641, A2
Planck Collaboration IV. 2018, A&A, 641, A4
Planck Collaboration XI. 2020, A&A, 641, A11
Planck Collaboration Int. LVII. 2020, A&A, 643, A42
Rubiño-Martín, J. A., Guidi, F., Génova-Santos, R. T., et al. 2023, MNRAS, 519, 3383
Svalheim, T. L., Andersen, K. J., Aurlien, R., et al. 2023a, A&A, 675, A14
Svalheim, T. L., Zonca, A., Andersen, K. J., et al. 2023b, A&A, 675, A9
Watts, D. J., Basyrov, A., Eskilt, J. R., et al. 2023a, arXiv e-prints, arXiv:2303.08095
Watts, D. J., Galloway, M., Ihle, H. T., et al. 2023b, A&A, 675, A16
Wehus, I. K., Fuskeland, U., & Eriksen, H. K. 2013, ApJ, 763, 138
Weiland, J. L., Addison, G. E., Bennett, C. L., Halpern, M., & Hinshaw, G. 2022, ApJ, 936, 24
Weiland, J. L., Osumi, K., Addison, G. E., et al. 2018, ApJ, 863, 161

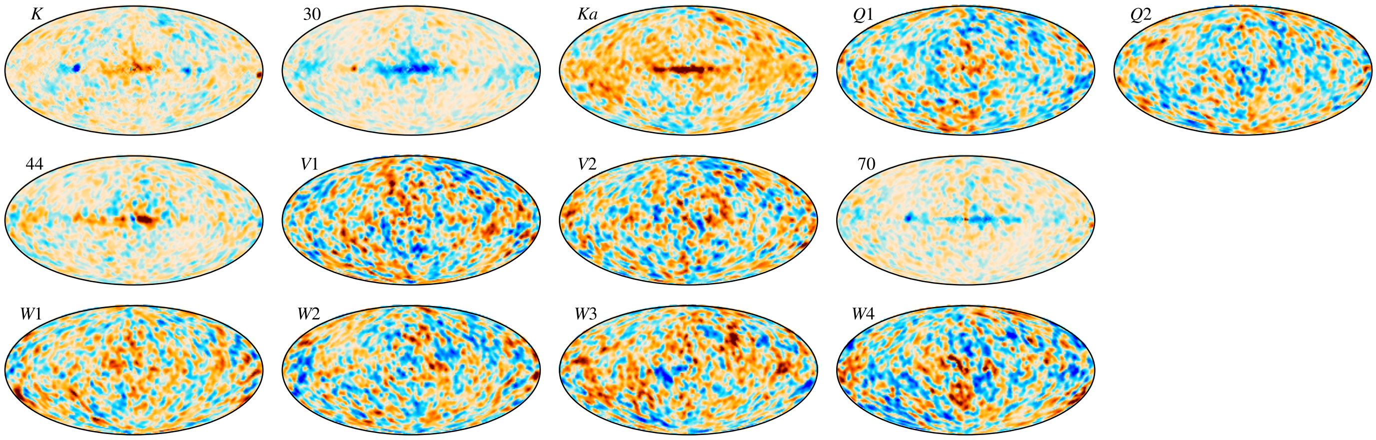

Fig. 11. Stokes Q residual maps. The color scale is $\pm5\,\mu$K for all bands except W, which are displayed with limits of $\pm10\,\mu$K.

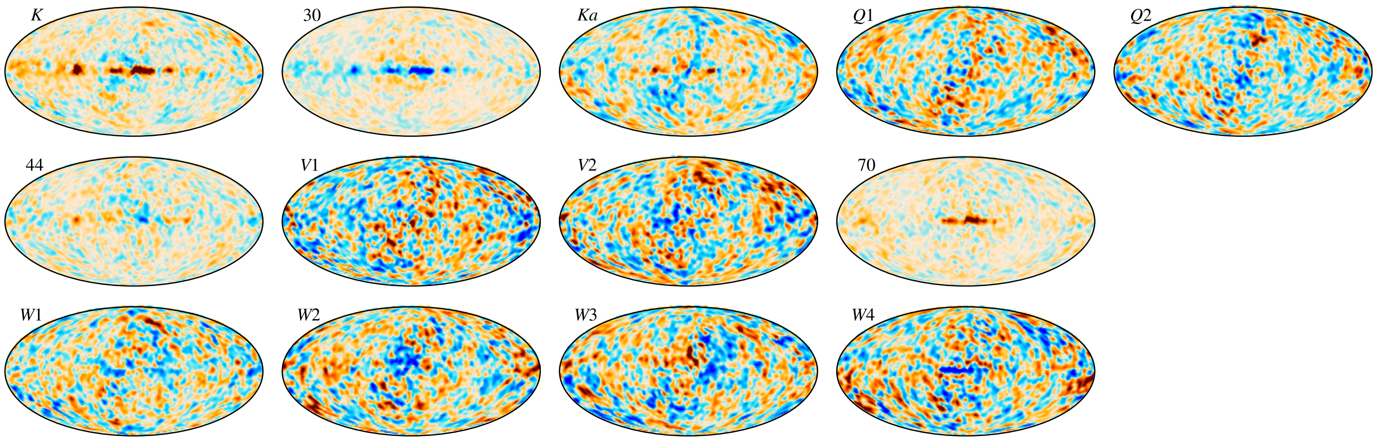

Fig. 12. Stokes U residual maps. The color scale is $\pm5\,\mu$K for all bands except W, which are displayed with limits of $\pm10\,\mu$K.

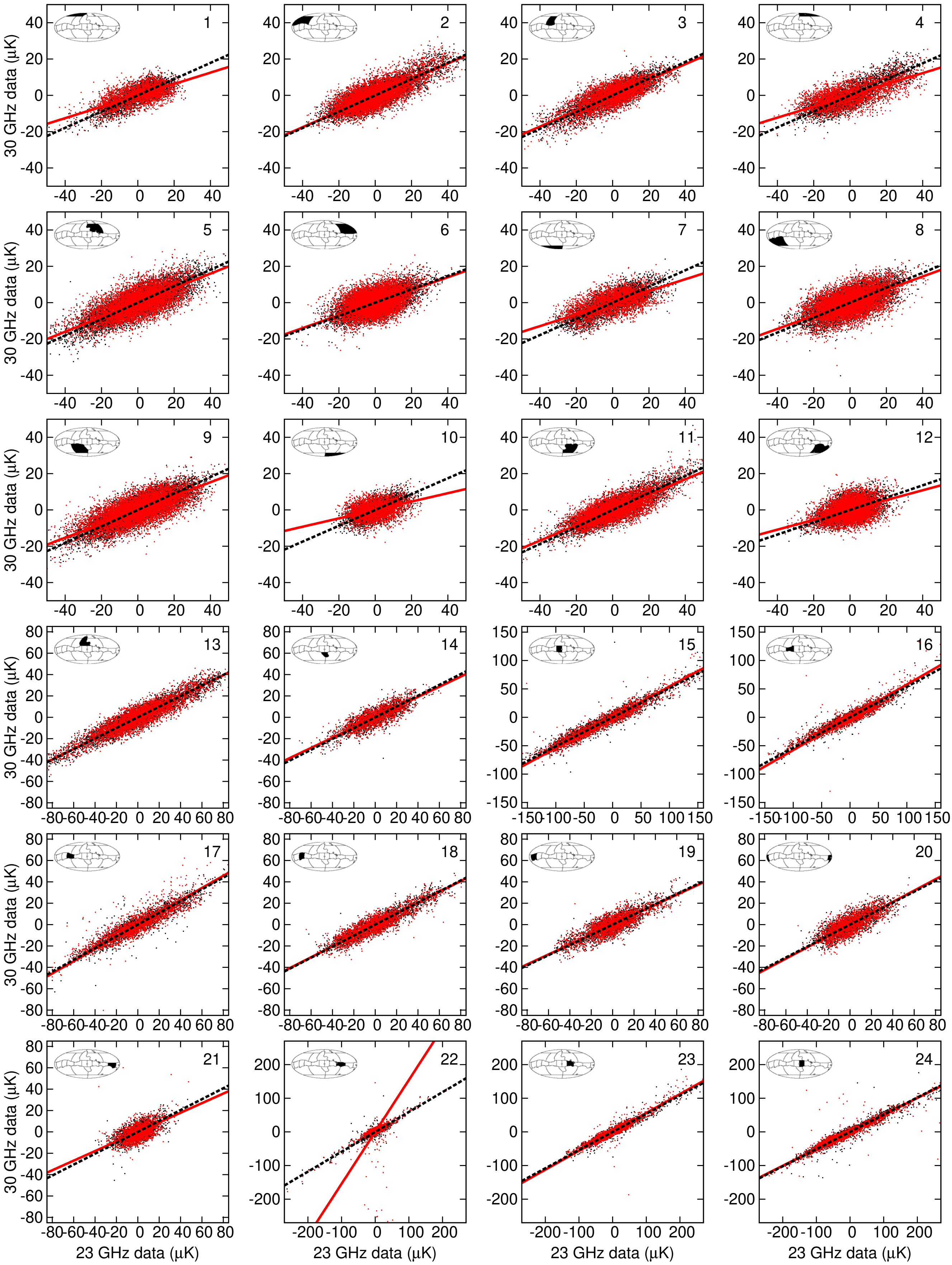

Fig. .1. T-T plots for Stokes Q and U maps of the COSMOGLOBE 23 GHz versus the COSMOGLOBE 30 GHz (black) and the 9 yr *WMAP* 23 GHz versus *Planck* 2018 30 GHz (red) for all regions. The horizontal (solid and dotted) lines indicates the corresponding inverse variance weighted values of the spectral index, averaged over rotation angle, and in the COSMOGLOBE case also samples.

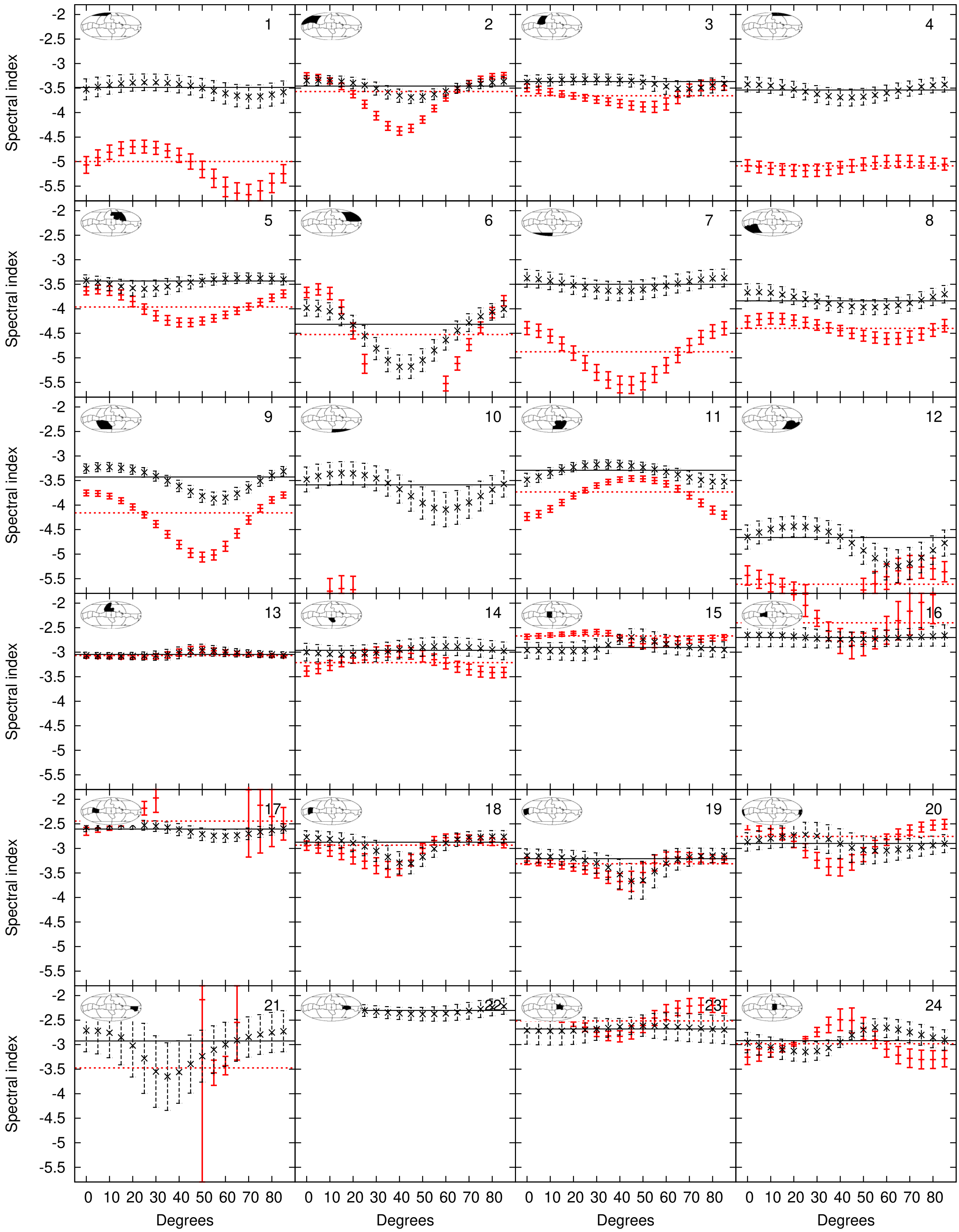

Fig. .2. The synchrotron spectral index as a function of rotation angle, computed using T-T plot between the COSMOGLOBE 23 GHz and the COSMOGLOBE 30 GHz (black) compared to the spectral index using the 9 yr *WMAP* 23 GHz and *Planck* 2018 30 GHz (red) for all regions. The horizontal (solid and dotted) lines indicates the corresponding inverse variance weighted values of the spectral index, averaged over rotation angle, and in the COSMOGLOBE case also samples.

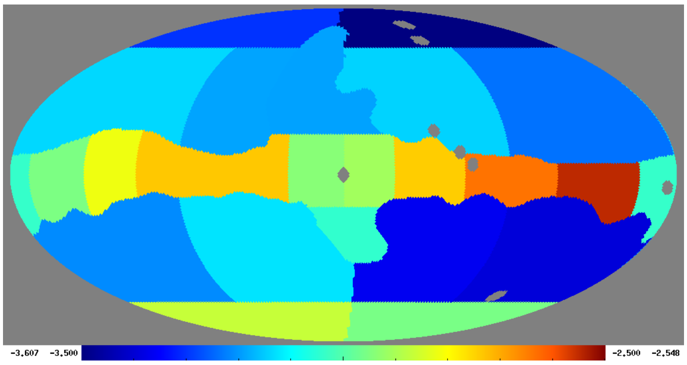

Fig. .3. The spatial variation of the synchrotron spectral index, computed using T-T plot between the Cosmoglobe *WMAP* *K*- and *Ka*-band. The spectral index is inverse variance weighted over rotation angle and samples. Fix style of maps.

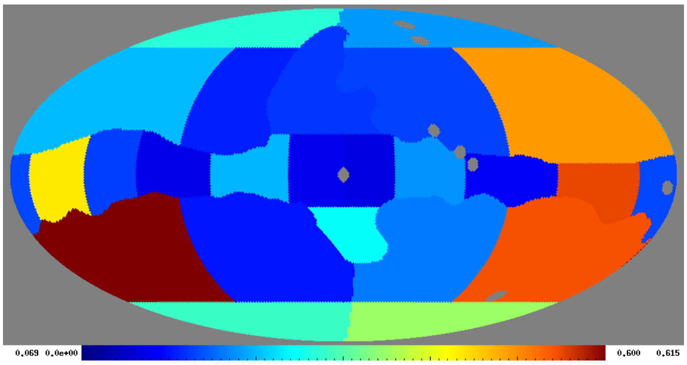

Fig. .4. The uncertainty of the synchrotron spectral index, computed using T-T plot between the Cosmoglobe *WMAP* *K*- and *Ka*-band. Fix style of maps if we keep it.

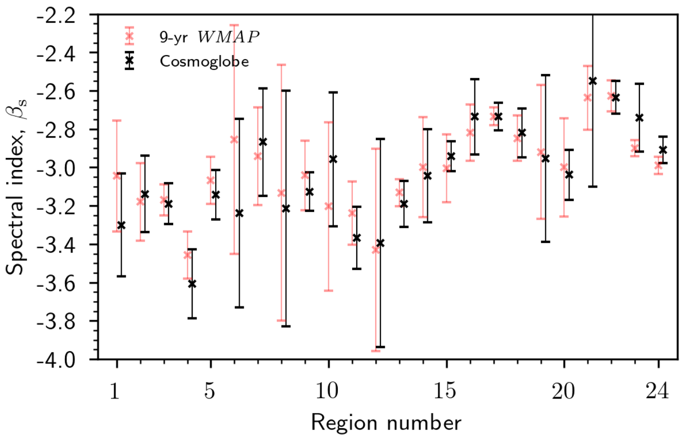

Fig. .5. The synchrotron spectral index, computed using T-T plot between the Cosmoglobe *WMAP* *K*- and *Ka*-band (black) compared to the spectral index using the original 9-yr *WMAP* data (red) as a function of region number. The spectral index is inverse variance weighted over rotation angles, and in the Cosmoglobe case also samples.

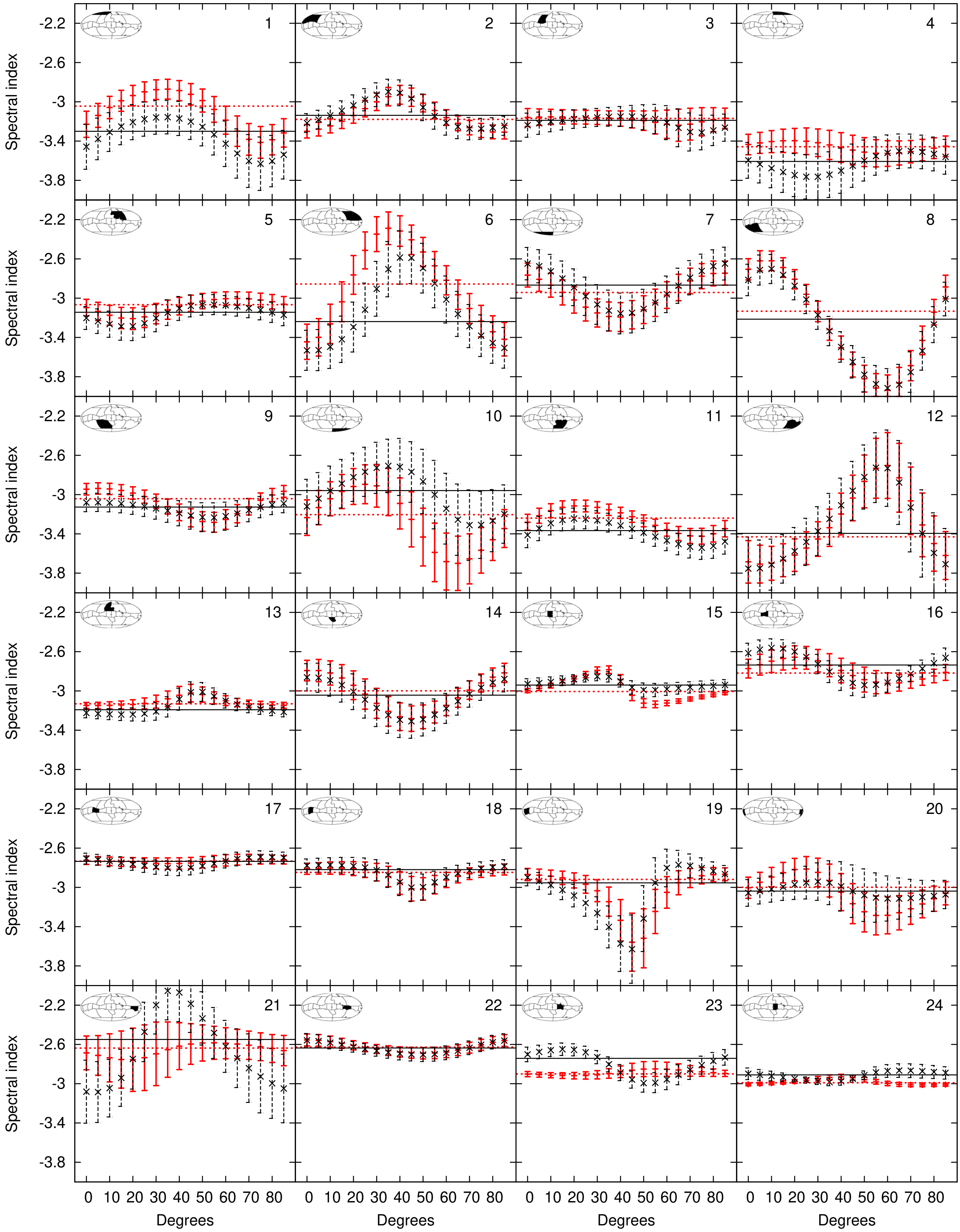

Fig. .6. The synchrotron spectral index as a function of rotation angle, computed using T-T plot between the Cosmoglobe *WMAP K*- and *Ka*-band (black) compared to the spectral index using the original 9-yr *WMAP* data (red) for all regions. The horizontal lines indicates the corresponding inverse variance weighted values of the spectral indiex.